

Improved Mapping of Tropospheric Delays

CHRISTIAN ROCKEN

GPS Science and Technology Program, UCAR, Boulder, Colorado

SERGEY SOKOLOVSKIY

GPS Science and Technology Program, UCAR, Boulder, Colorado, and A. M. Obukhov Institute of Atmospheric Physics, Moscow, Russia

JAMES M. JOHNSON AND DOUG HUNT

GPS Science and Technology Program, UCAR, Boulder, Colorado

(Manuscript received 17 July 2000, in final form 21 November 2000)

ABSTRACT

The authors compare several methods to map the a priori tropospheric delay of global positioning system (GPS) signals from the zenith direction to lower elevations. This is commonly achieved with so-called mapping functions. Dry mapping functions are applied to the hydrostatic delay; wet mapping functions are used to map the zenith wet delay to lower elevation angles. The authors compared the following mapping techniques against raytraced delays computed for radiosonde profiles under the assumption of spherical symmetry: (a) the Niell mapping function; (b) mapping through the COSPAR International Reference Atmosphere with added water vapor climatology; (c) the same as b with added use of surface meteorological temperature, pressure, and humidity; and (d) use of the numerical reanalysis model of the National Centers for Environmental Prediction–National Center for Atmospheric Research. Based on comparisons with all available global radiosondes (~ 1000 per day), for every fifth day of 1997 (73 days), the authors found that dry mapping based on method d performs 2–3 times better than a for elevations 15° and below. The authors further report that b and c perform better dry mapping than a, with an improvement of $\sim 50\%$. Smaller improvements are also shown for wet delay mapping by b, c, and d as compared to a. At 5° and below, the Niell dry mapping function has biases that vary with season by 1%, and it displays significant systematic errors (2%–4% at 5° elevation) between 30° and 90° southern latitude during the northern winter months. It is concluded that the most demanding meteorological and geodetic GPS applications should use location- and time-specific “direct” mapping functions such as b, c, or d rather than parameterized functions, especially if low elevation observations are used. The authors describe how this improved mapping can be implemented in GPS analysis software.

1. Introduction

High-precision scientific applications of the global positioning system (GPS) in geodesy and meteorology require corrections for the delay of the signal in the neutral atmosphere. The atmospheric delay is generally divided into its hydrostatic or dry and wet components (Davis et al. 1985). The line of sight delay for these components is described as the zenith delay multiplied by the mapping function, which defines the dependence on elevation angle. In practice, the zenith dry delay is often computed based on Saastamoinen’s (1972) hydrostatic delay correction, which is just a function of surface pressure. This delay is then mapped to lower elevation angles using one of several well-known mapping functions. The Niell mapping function (Niell 1996) is

most commonly used in space geodesy because it is presently believed to be the most accurate at elevation angles below 10° and it does not require any meteorological observations. The zenith wet delay is commonly estimated simultaneously with other parameters such as clock offsets, GPS satellite orbits, and geodetic positions.

There is a tendency to take GPS observations to ever lower elevation angles because low elevation data improve the observation geometry, increase the amount of available data, and contain interesting meteorological information. Low-elevation GPS slant observations are of particular interest in meteorology (Ware et al. 1997; Flores et al. 2000; Braun et al. 2000; MacDonald and Xie 2000). There is also increasing interest in the near-horizon observations because they contain atmospheric profile information (Sokolovskiy et al. 2000; Lowry et al. 2000, manuscript submitted to *Radio Sci.*, hereafter LOW). To process such near-horizon GPS observations,

Corresponding author address: Dr. Christian Rocken, COSMIC and GST Programs, UCAR, 3300 Mitchell Lane, Boulder, CO 80301.
E-mail: rocken@ucar.edu

for the estimation of the carrier cycle ambiguities and for cycle slip repair, good mapping functions are required. As we will show below, especially at low elevations angles (7° or less), even the best mapping function currently in use can introduce significant errors.

We therefore investigated a concept that we will call direct mapping. Direct mapping differs from parameterized mapping functions such as the Niell mapping function (NMF) in that it requires an atmospheric profile of temperature, pressure, and humidity for a specific location and time. Such a profile can be obtained from climatology or from numerical weather analysis fields, which are interpolated to the specific location of the GPS receiver and to the specific date of the GPS data. Based on this profile, we compute the site- and date-specific mapping function by computing delays as a function of elevation angles using ray integrals under the assumption of spherical symmetry. This location- and time-specific direct mapping function can then be used for the analysis of GPS data. Atmospheric profiles are obtained from a climatological model CIRA86a-Q-UoG (Kirchengast et al. 1999), called just CIRA-Q below, and from the National Centers for Environmental Prediction–National Center for Atmospheric Research (NCEP–NCAR) 40-Year Reanalysis (Kalnay et al. 1996). Mapping functions based on these two sources of atmospheric profiles and the NMF mapping were compared to mapping functions computed from global radiosondes during 1997. Typically, there were ~ 1000 radiosondes available each day, and we computed comparisons for each of those approximately 1000 cases for every fifth day of 1997. Statistical comparisons over the range of latitudes and the period of 1 yr are shown below.

2. Obtaining the meteorological data profiles

First, we obtain all available radiosonde observations from NCAR. For the time and location of each of these radiosonde files, we obtain the corresponding profile from the NCEP–NCAR 40-Year Reanalysis. The reanalysis provides gridded data with 17 pressure levels ranging from 1000 to 10 mb. Horizontal and temporal resolution are 2.5° in longitude and latitude and 6 h, respectively. We use geopotential heights, pressure, temperature, and humidity from this dataset. To obtain the values of the reanalysis, spatial and temporal interpolations are required. Two grids are selected, one for the model time before and one for the model time after the radiosonde launch. Latitude and longitude are taken from the fixed location of the radiosonde release site. A value for each model level is determined by two-dimensional interpolation using the 16 gridpoint values surrounding the radiosonde location. Taking these values for each level of the analysis yields a vertical profile at the 6-h time boundaries immediately before and after the radiosonde release. These two profiles are then interpolated linearly to the radiosonde release time. Since

standard radiosonde release times usually coincide with available model output times, temporal interpolation is not required for this study. However, our software is configured to extract profiles from the gridded model fields at arbitrary times and locations.

The CIRA-Q climatological tables contain values of pressure and temperature between 0 and 120 km. These values are provided at 1-km levels from 0° to 15° km and at 5-km levels above, with 10° resolution in latitude and monthly temporal resolution. The tables also contain specific humidity at 1-km levels between 0 and 15 km with the same $10^\circ \times 1$ -month latitude and temporal resolution. To obtain the CIRA-Q values corresponding to a radiosonde dataset, the tables are interpolated linearly in space and time. The uncompressed ASCII table of CIRA-Q requires 0.17 MB disk storage, and this climatology can easily be read into computer memory by a GPS data analysis program.

3. Determination of direct mapping functions

Once a profile of temperature T (degrees kelvin), pressure P (mb) and water vapor pressure e (mb) as a function of geometric height, has been obtained from radiosondes, CIRA-Q, or NCAR–NCEP, we compute the delay on a fine grid of 900 elevation angles between 90° (zenith) and 0° . First, we determine the refractivity $N = (n - 1)10^6$, where n is the index of refraction at each height layer from radiosonde or model data. We use an expression by Davis et al. (1985), who rewrote the refractivity determined by Thayer (1974) as

$$N = k_1 R_d \rho + k_2' \frac{e}{T} Z_w^{-1} + k_3 \frac{e}{T^2} Z_w^{-1}. \quad (1)$$

Here, ρ is the density of (moist) air, R_d is the specific gas constant for dry air, and the other constants are given by Davis et al. (1985) as $k_1 = 77.604 \text{ K mb}^{-1}$, $k_2' = 17 \text{ K mb}^{-1}$, and $k_3 = 377\,600 \text{ K}^2 \text{ mb}^{-1}$. The inverse compressibility of moist air Z_w^{-1} is defined (Ownes 1967) as

$$Z_w^{-1} = 1 + 1650 \left(\frac{e}{T^3} \right) (1 - 0.01317t + 1.75 \times 10^{-4}t^2 + 1.44 \times 10^{-6}t^3), \quad (2)$$

where t is the temperature ($^\circ\text{C}$). The density of air can be computed as

$$\rho = \frac{P}{R_d T_v}, \quad (3)$$

where T_v is the virtual temperature, which is related to temperature by $T_v = T(1 + 0.608s)$. Here, s is the specific humidity of air, which is related to e by (Matveev 1967)

$$s = \frac{0.622e}{P - 0.378e}. \quad (4)$$

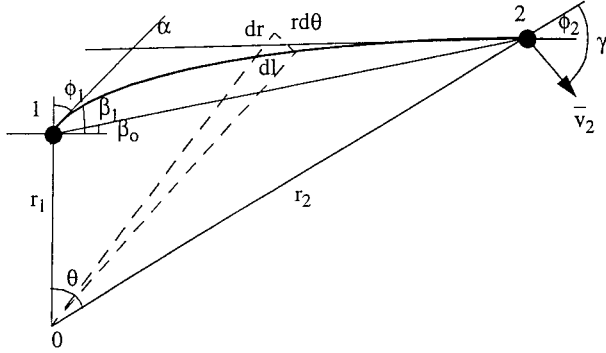


FIG. 1. Shows the geometry of a ray (thick line from transmitter 2 to receiver 1 for the computation of the refractive integrals.

The first term on the right-hand side of Eq. (1) is defined as the dry refractivity N_d , the sum of the remaining two terms on the right-hand side of Eq. (1) is defined as the wet refractivity N_w .

Above the top height of the radiosondes or model output, we use CIRA_Q refractivities, also interpolated in space and time from the monthly tabular values, up to 120 km. Refractivities are then log-linearly interpolated onto a high-density altitude grid. With this representation of refractivity, the ray integrals are estimated following a well-known technique (e.g., Kelso 1964; Kravtsov and Orlov 1990). The delay S of the signal between points 1 (i.e., the GPS receiver at the radio-sonde release site) and 2 (a GPS satellite at 26 550-km altitude) is

$$S = \int_1^2 n \, dl. \quad (5)$$

As can be seen from Fig. 1, in polar coordinates (r, θ) , the path segment is equal to $dl = \sqrt{dr^2 + r^2 d\theta^2}$. We use Bouger's law

$$a = rn \sin \phi = rn \frac{rd\theta}{dl}, \quad (6)$$

where ϕ is the angle between the ray and the radial direction and a is the impact parameter of the ray. This allows us to eliminate $d\theta$ and to arrive at the expression for the phase delay S :

$$S = \int_{x_1}^{x_2} \frac{(1 - xm')x \, dx}{\sqrt{x^2 - a^2}}, \quad (7)$$

where $x = rn$, $m = \ln[n(x)]$, and $m' = d \ln n / dx$. We define $n_d = 1 + 10^{-6} N_d$ as the dry index of refraction and $n_w = 10^{-6} N_w$ the wet index of refraction, so that $n_d + n_w = n$. Further, we define S_0 as the distance between points 1 and 2. The calculation of S_0 for a given impact parameter a is discussed in the appendix. The excess phase due to the dry part, ΔS_d , and wet part, ΔS_w , of the atmosphere can be computed according to

$$\Delta S_d = \int_{x_1}^{x_2} \frac{\frac{n_d}{n}(1 - xm')x \, dx}{\sqrt{x^2 - a^2}} - S_0, \quad (8a)$$

$$\Delta S_w = \int_{x_1}^{x_2} \frac{\frac{n_w}{n}(1 - xm')x \, dx}{\sqrt{x^2 - a^2}}. \quad (8b)$$

The path that is traveled by the signal is determined by the full index of refraction n . The integral in Eq. (8a) includes the geometric excess path due to bending plus the effect of slowing due to the dry atmospheric refractive index. The integral in (8b) includes only the effect of slowing due to the wet refractivity along the signal path. This follows the definition of dry and wet signal delay that was also used by Davis (1985) and Niell (1996). We numerically calculate these integrals with an integration step size of 10 m between 0 and 2 km, 20 m between 2 and 6 km, 50 m between 6 and 16 km, 100 m between 16 and 36 km, and 500 m between 36 and 136 km. We verified that this selection of integration steps yields nearly identical results (submillimeter agreement at 1° elevation) to use a 5-m integration for the entire height range. We also validated our numerical integration against the case of a linear function $m(x)$ for which integral (7) can be solved analytically and found excellent agreement. We also compared the results from integrals (8a,b) with a 3D raytracing algorithm using the Runge–Kutta method and found agreement at the 2-mm level at 0° elevation. In summary, extensive tests were conducted to validate our computation of the excess path delay. While integrals (7) and (8a,b) can be applied to a spherically symmetric atmosphere only, they are computationally faster than 3D raytracing and thus suitable for direct mapping applications within the GPS analysis software.

The signal bending α is computed according to (see appendix for details)

$$\alpha = -a \int_{x_1}^{x_2} \frac{m' \, dx}{\sqrt{x^2 - a^2}}. \quad (9)$$

Because of this bending, the arrival elevation angle of a signal, especially at low angles is larger than the geometric angle of a straight line to the GPS satellite. In GPS analysis, the mapping function must provide a delay correction as a function of the geometric angle. As discussed in the appendix, we do not use a shooting or iterative technique to find the arrival angle for a specified geometric angle. Instead we compute the associated geometric angles for a dense grid of 900 arrival angles (all angles 0° – 90° in 0.1° increments) and then apply a cubic spline interpolation to obtain the delays associated with any specified geometric angle (see the appendix for a more detailed description). For this study, we obtained results for geometric elevations of 90° , 15° , 10° , 7° , 5° , 3° , and 1° . The mapping is then computed as the

ratio of the excess phases ΔS in the oblique and zenith directions:

$$M_d(j) = \frac{\Delta S_d(j)}{\Delta S_d(1)}, \quad (10a)$$

$$M_w(j) = \frac{\Delta S_w(j)}{\Delta S_w(1)}, \quad (10b)$$

where d and w again denote the hydrostatic or wet cases respectively, and j is the index corresponding to the geometric elevation angle with $j = 1$ representing the zenith case. As an example, a typical hydrostatic (dry) excess delay value for a site at sea level is 2.3 m at 90° and 23 m at 5° ; thus, the value of the mapping function at 5° is 10. The wet zenith delay varies greatly in the range from 0 to 50 cm due to the variability of atmospheric water vapor. Because the atmospheric water vapor scale height is several times smaller than the dry tropospheric scale height (~ 8 km), it also maps differently. Generally, wet mapping functions are larger than the dry mapping functions and much more variable.

The NMF was computed according to the paper by Niell (1996). Mapping using CIRA-Q was computed for two variations: 1) CIRA-Q climatology was used (we refer to this as CMF in the following) and 2) we used the surface meteorological values (taken from the lowest radiosonde observation) and CIRA-Q above 4 km. The refractivities between the surface value and the 4-km CIRA-Q value were obtained by log-linear interpolation. We will refer to mapping with this combined CIRA-Q plus surface data as CSMF. The NCEP-NCAR-based mapping will be referred to as NNMF. Finally, the radiosonde-based mapping will be called RMF.

We consider RMF as the truth and compare it with NMF, CMF, CSMF, and NNMF. To continue our 5° example, if the hydrostatic mapping based on RMF yields 10.0 and CMF maps at 10.01, then this difference is interpreted as an error of 0.01 in the CMF mapping function for this particular profile. This error, caused by using the hydrostatic CMF, corresponds to a delay error of $\sim 0.01 \times 2.3$ m or 1% of the zenith delay. This mapping error would affect a low elevation 5° GPS slant delay observation of atmospheric water vapor directly at the 2.3-cm level. Using the approximate conversion factor of 6.5 to relate signal delay and water vapor (e.g., Bevis et al. 1992), this is equivalent to 0.35 cm of integrated water vapor in the slant direction. Neill (1996) states that for geodetic analysis of GPS and VLBI observations in which site position, atmospheric delay, and site clocks are estimated, the error in geodetic height is smaller by a factor of approximately 0.3 than the path-length error at 5° minimum elevation. MacMillan and Ma (1994) provide similar factors over a range of minimum elevations from 1° to 10° . Their published values change nearly linearly from 0.1 at 1° and 0.22 at 5° to 0.41 at 10° . Thus, if we average the values published by Niell (1996) and MacMillan and Ma (1994), we see

that the 2.3-cm error of the CMF dry mapping function example would cause a geodetic position height error of ~ 6 mm. Horizontal positioning errors due to mapping function uncertainties are much smaller than vertical errors for good observation geometries.

4. Results

In Fig. 2, we show the comparison of radiosondes and the different mapping techniques. The left four panels show the dry mapping for 1 January 1997, and the right panels show the wet mapping. In each panel, we also list the bias and the standard deviation about this bias of the comparisons. Each dot in these figures corresponds to a radiosonde launch. For the dry mapping, we see that there is a slight improvement of the CIRA mapping versus the NMF on this day. Dry mapping with NNMF is clearly superior to the other three techniques. The dry NMF shows a bias in the Southern Hemisphere of up to almost -4% (~ -8 cm). This bias (which is systematic during the northern winter days) is not seen with any of the other mapping techniques.

The wet mapping functions are noisier, as should be expected because of the high variability in the distribution of atmospheric water vapor (note the difference in scale between the left and the right panels). The NNMF mapping function performs the best with a small bias and a standard deviation of about 7%. Note that this is 7% of the zenith wet delay. The zenith wet delay is very variable, but if we assume an average wet delay of ~ 20 cm for this day, then this 7% standard deviation corresponds to ~ 1.4 cm. Both NMF and CSMF have significant biases on this day.

Figure 3 summarizes the dry and wet mapping biases and standard deviations for the four techniques that were compared to the radiosondes at 5° for the entire year. Each symbol on this figure corresponds to the bias and standard deviation based on about 1000 daily global radiosonde launches, as shown in Fig. 2. For the dry mapping, the figure shows that the NNMF has smaller bias and standard deviation and a much reduced seasonal dependence than the other three mapping techniques. Both CSMF and, to a lesser extent CMF perform generally better than NMF. Both CMF and NNMF have significantly smaller biases and also reduced seasonal dependence compared to NMF. The wet mapping for NMF has a significant bias of almost -5% for the Northern Hemisphere winter months.

Tables 1 and 2 summarize all the mapping function results and the improvements of the three direct mapping techniques in comparison to the parametric NMF technique. Column 1 shows the elevation angle. The next two columns of each table show the bias (column 2) and standard deviation (column 3) obtained from the global comparison of NMF with all available radiosondes over the period of 1 yr. The biases shown in Tables 1 and 2 are the averages of the absolute value of the biases plotted in Fig. 3. This was done to avoid

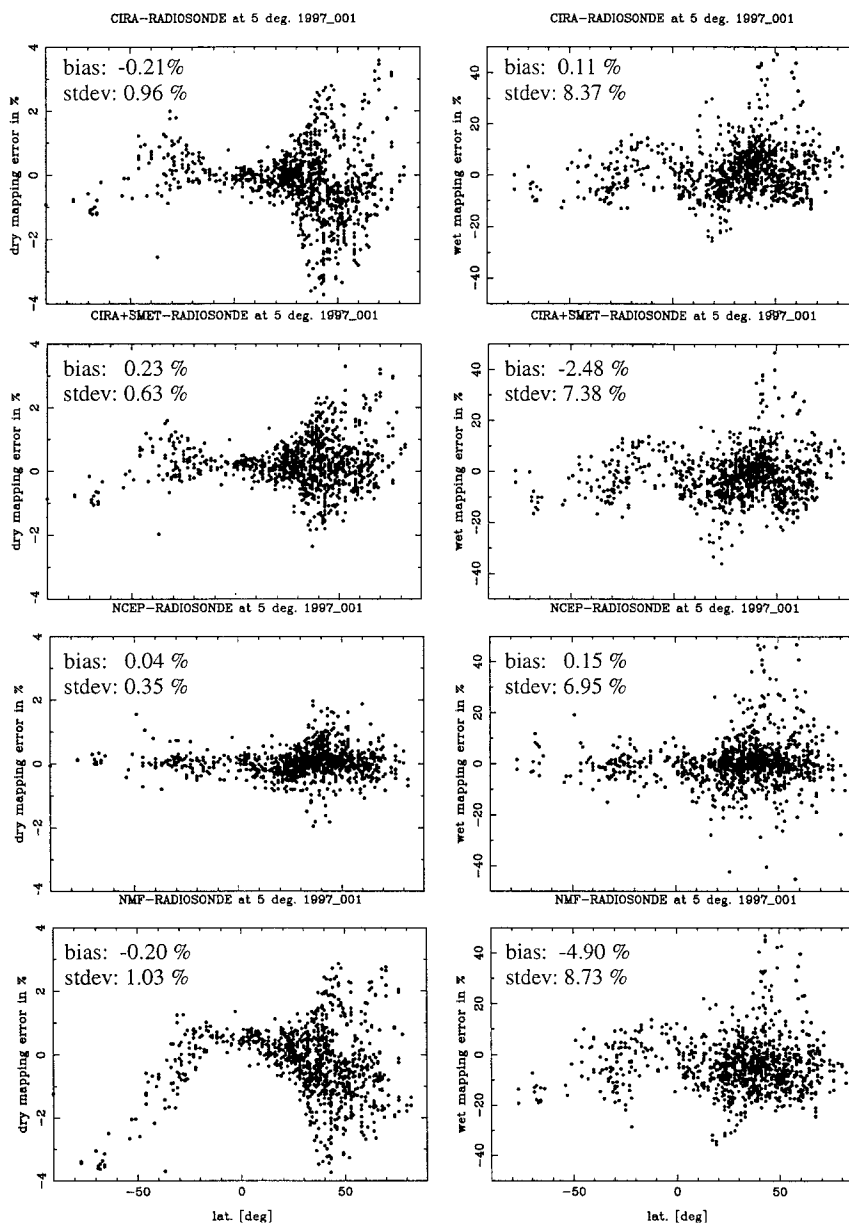


FIG. 2. Mapping function comparison for 1 Jan 1997. The four panels on the left (right) compare the dry (wet) mapping functions at 5° elevation for CMF, CSMF, NNMF, and NMF (top to bottom). Each dot represents the difference, with mapping based on a radiosonde launch. This difference is shown in % of the zenith dry (wet) delay as a function of geodetic latitude. Global bias and std dev of the differences with radiosonde mapping are given in each panel.

averaging biases that may change from positive to negative during the year. The subsequent columns (4–9) show the ratio of the NMF bias and standard deviation to the bias and standard deviation from the direct mapping techniques. These values (if larger than 1) are the improvement factors compared to NMF. For example, in Table 1, the value of 1.4 in the CSMF standard deviation improvement (column 7) at 5° means that the standard deviation is on average improved by a factor of 1.4 using CSMF compared to NMF. Since the NMF

dry mapping standard deviation is 0.95% (~ 2.3 cm) at 5° , the corresponding CSMF value is 0.69% (1.6 cm). The most significant improvements in both bias and standard deviation are achieved with the NNMF mapping function. Improvements for the wet mapping function are smaller, but even here, the bias can be reduced on average by almost a factor of 2 at the lowest elevation angles with the NNMF and by a factor of 1.7 with CSMF. The very large improvements by all three direct mapping techniques at 1° are not surprising, since NMF

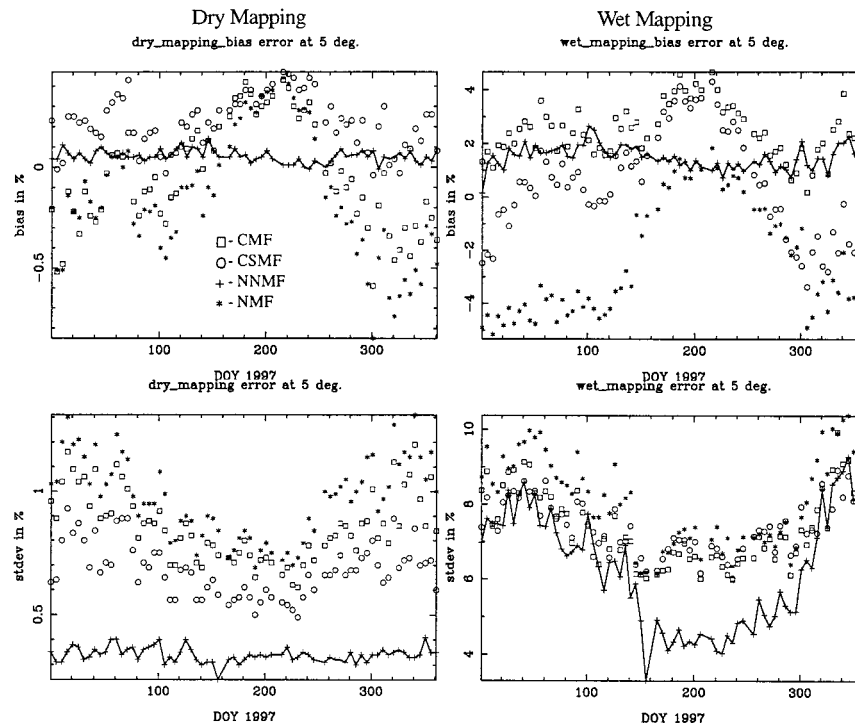


FIG. 3. Shows the global averages of the bias (top panels) and std dev (bottom panels) for the dry (left panels) and wet (right panels) mapping functions compared to radiosonde mapping. The NNMF results are connected by a line. These comparisons are for mapping at 5° for 1997.

was never meant to be applied below 3°. The large apparent improvement in the dry NNMF bias at 15° will not have a significant effect on most applications because the NMF bias of 0.03% is already small, corresponding to 0.07 cm of delay.

5. Discussion of results

Those applications of the GPS that use low-elevation observations can benefit from direct mapping functions. The greatest benefit results from the use of a numerical analysis, but even the modified CIRA_Q climatology with or without added surface meteorological values

reduces biases and the standard deviation compared to NMF.

Since CMF and NMF are both based on climatology, it is not immediately obvious why CMF performs somewhat better (improvement in dry mapping bias seems significant, while the improvement in standard deviation of the dry and wet mapping functions is about 10%). There are two possible explanations: 1) the CIRA_Q climatology may be more representative of the global atmosphere than the profiles of the *U.S. Standard Atmospheres* for north latitudes that were used to develop NMF (Neill 1996) or 2) no additional parameterization of the CIRA_Q climatology is required, since we inter-

TABLE 1. Dry mapping with NMF and improvement of direct mapping techniques. The values shown are global annual averages. The two columns on the left are the bias and std dev for NMF in percent. For approximate conversion to path delay, multiply these values by 2.3 cm. The other values are comparisons with NMF. Values larger than 1 are improvements. For conversion to path delay, divide the corresponding NMF bias or std dev (converted to path delay) by these values.

Elev	NMF bias (%)	NMF std dev (%)	Improvement factors compared to NMF					
			CMF bias	CMF std dev	CSMF bias	CSMF std dev	NNMF bias	NNMF std dev
15°	0.03	0.05	2.2	1.1	2.7	1.4	36.2	2.6
10°	0.06	0.17	1.5	1.1	1.8	1.4	6.4	2.8
7°	0.13	0.43	1.3	1.1	1.4	1.4	5.8	2.9
5°	0.30	0.97	1.3	1.1	1.3	1.4	5.4	2.9
3°	0.73	2.7	1.2	1.1	1.0	1.4	4.4	2.9
1°	37.6*	11.3*	15.0	1.2	9.8	1.7	48.4	3.2

* Note that NMF should not be used below 3°.

TABLE 2. Same as Table 1 for the wet mapping functions. For approximate conversion to path delay, multiply these values by 0.2 cm. The other values are comparisons with NMF. Values larger than 1 are improvements. For conversion to path delay, divide the corresponding NMF bias or std dev (converted to path delay) by these values.

Elev	NMF bias (%)	NMF std dev (%)	Improvement factors compared to NMF					
			CMF bias	CMF std dev	CSMF bias	CSMF std dev	NNMF bias	NNMF std dev
15°	0.12	0.38	1.0	1.1	1.6	1.1	1.6	1.3
10°	0.40	1.24	1.0	1.1	1.6	1.1	1.6	1.3
7°	1.10	3.36	1.0	1.1	1.7	1.1	1.7	1.3
5°	2.77	8.13	1.1	1.1	1.7	1.1	1.9	1.3
3°	9.53	26.73	1.3	1.1	1.7	1.1	2.2	1.3
1°	43.0*	150.98*	1.4	1.1	1.2	1.1	2.1	1.3

* Note that NMF should not be used below 3°.

polate that climatology for a given date and location, while the NMF involves a best fit to a limited number of mapping function parameters. The further improvement of CSMF over NMF is due to the added input of surface meteorological measurements. Clearly, this is an added complication for data collection and analysis.

Finally, the use of the output of numerical weather models to compute direct mapping functions provides the most dramatic improvement over NMF. Numerical weather models are primarily driven by radiosonde data, and therefore the comparison between radiosonde mapping and NNMF is not completely independent. However, these models have been verified by independent measurement techniques (e.g., Rocken et al. 1997a) and are believed to provide the state-of-the-art representation of the atmosphere.

To implement any of the direct mapping functions (CMF, CSMF, or NNMF) within the GPS analysis software, we should estimate the mapping upon the first request for a delay correction for a specific GPS site. Mapping can be computed on a dense grid of elevations and represented by spline or polynomial coefficients. These coefficients can then be used to determine the mapping of the zenith correction each time a delay correction has to be computed for a specific station and GPS satellite.

In the case of the CSMF, the surface meteorological measurements also have to be provided. These values change with time. However, the influence of this change on the dry mapping function can be considered small, and the direct mapping functions, suitable for many hours of GPS data, can be computed based on initial or average surface meteorological values. Since surface meteorological data are commonly available for GPS sites that are operated for meteorology, use of CSMF is generally possible.

Implementation of the NNMF requires access to profiles from the numerical data analysis. In the near future, such site- and data-specific profiles could be provided via the Internet to the GPS analysis center in much the same way that orbits and earth orientation parameters are supplied today. If the use of direct mapping functions like NNMF becomes more widely accepted, a service

can be provided to instantly return a profile, in a standard format, via the Internet. The user would then compute the site- and date-specific NNMF mapping functions based on these profiles. For real-time application (Rocken et al. 1997b; Ware et al. 2000), it is also feasible that profiles based on predicted fields are provided, rather than those based on the reanalysis used in this paper.

The zenith hydrostatic delay should still be computed according to the formulation of Saastamoinen, modified by Davis (1985), and mapped to lower elevation angles by the direct mapping functions.

Observed improvements for the wet mapping functions were quite small (even for NNMF). In addition, the assumption of azimuthal-spherical symmetry in the water vapor distribution is generally not valid, especially at low elevation angles. Small-scale variations in the water vapor field are not resolved by weather analysis fields with 10–30 km horizontal resolution. Improvements in wet mapping are therefore hard to achieve, even if 3D fields and raytracing were used, because the required water vapor information is not available. We therefore suggest to continue to use the NMF wet mapping for the estimation of the wet delay after the hydrostatic delay has been corrected by use of one of the direct mapping functions discussed above.

6. Conclusions

Extensive comparison of the performance of several mapping techniques shows that better calibration of the a priori tropospheric delay can be achieved with direct mapping as compared to use of a parameterized mapping function such as the NMF. Especially direct mapping of the hydrostatic delay based on numerical weather models reduces delay errors due to mapping significantly at all elevation angles below 15°. Furthermore, the direct mapping with the CIRA-Q climatology and with the NCAR–NCEP reanalysis significantly reduces seasonal and latitudinal biases that we observed for the NMF.

Three-dimensional raytracing through high-resolution weather analysis fields (e.g., Chen and Herring 1997) can be expected to outperform direct mapping, as defined in this paper, because it does not depend on

the assumption of spherical symmetry in the refractive index. Obtaining and interpolating the weather fields and raytracing, however, would add significant complexity and computational expense to the GPS data analysis. Direct mapping, as described in this paper, is a compromise between parametric mapping functions and 3D raytracing that is relatively simple to implement, computationally fast, and shows significant improvement at the lowest elevations.

The effect of direct mapping on geodetic observations with GPS has not yet been investigated because this research was motivated by the need for better mapping of the near-horizon signal delay for meteorological applications. Such low-elevation observations can be taken for the detection of atmospheric ducting conditions (LOW) and for the measurement of refractive signal bending near the horizon (Sokolovskiy et al. 2000). Line-of-sight observations of signal delay in the direction to the GPS satellites can be used to measure atmospheric inhomogeneity due to water vapor (Ware et al. 1997) if the hydrostatic delay can be removed. Hydrostatic delay calibration with the NNMF direct mapping function can in some cases reduce errors at 5° by as much as 8 cm over NMF (Fig. 2, southern latitudes) and should therefore be used in meteorological GPS applications where the water vapor-induced slant GPS delay is an observable (Ware et al. 1997; Braun et al. 2000; Flores et al. 2000; Mac Donald et al. 2000).

Acknowledgments. This work was supported by the Office of Naval Research 322 MM, Dr. S. Sandgathe, and by the DOE ARM program.

APPENDIX

Computation of the Bending Angle, Geometric Elevation, and Excess Phase

This section will use the same notation as shown in Fig. 1. Repeating Eq. (4) from above, the expression for the phase delay S is

$$S = \int_{x_1}^{x_2} \frac{(1 - xm')x \, dx}{\sqrt{x^2 - a^2}}, \quad (\text{A1})$$

where $x = rn$, $m = \ln n(x)$, $m' = d \ln n / dx = dm/dx$. In our calculations, r is related to the geometric height (obtained from the radiosondes, CIRA-Q, or NCEP-NCAR) through the local radius of curvature of the reference ellipsoid at the receiver site (or radiosonde release site). This radius of curvature depends on the azimuth due to earth's oblateness. It is maximal in latitudinal (E-W) and minimal in the longitudinal (N-S) directions. We always calculate this radius of curvature in the azimuth direction of 45° from north. (The selection of 45° for this study can introduce an error in the radius of curvature for GPS signals that arrive from a different azimuthal direction. This error, which is largest at the equator and zero at the poles, is small and has

been ignored in this study.) The impact parameter a of the ray is related to the elevation angle β_1 of the ray at the receiver according to

$$\beta_1 = \frac{\pi}{2} - \phi_1 = \frac{\pi}{2} - \arcsin\left(\frac{a}{n_1 r_1}\right), \quad (\text{A2})$$

where n_1 is the index of refraction at the receiver. After S is calculated for a given β_1 , x_1 , x_2 , we carry out the following two steps. First, the geometric elevation angle β_0 of the transmitter, as seen from the receiver, has to be computed. Second, the excess phase $\Delta S = S - S_0$, where S_0 is the distance between the receiver and the GPS transmitter, has to be computed. The excess phase as a function of the geometric angle of the transmitter $\Delta S(\beta_0)$ is required for the computation of mapping functions. Since it is not possible to calculate $\Delta S = S - S_0$ for a given arbitrary geometric elevation angle β_0 , we first calculate S , β_0 , and S_0 for a dense grid of corresponding β_1 and then obtain $\Delta S(\beta_0)$ by means of interpolation. To do this, we first have to compute the bending angle α of the ray for that grid β_1 :

$$\alpha = \int_1^2 \frac{dl}{R_c}, \quad (\text{A3})$$

where

$$dl = dr\sqrt{1 + r'^2/r^2}, \quad (\text{A4})$$

where $r' = dr/d\theta$ and R_c is the local radius of curvature of the ray, which can be expressed in polar coordinates (Korn and Korn 1961) as:

$$R_c = \frac{(r^2 + r'^2)^{3/2}}{(r^2 + 2r'r'' - rr''')}, \quad (\text{A5})$$

where $r'' = d^2r/d\theta^2$. To obtain the expression for bending α in the form of an integral similar to Eq. (7), we have to use Bouger's law to eliminate r' and r'' from the expressions for dl and R_c . As follows from Bouger's law,

$$r' = \left(\frac{r}{a}\right)\sqrt{r^2n^2 - a^2}. \quad (\text{A6})$$

Differentiation of (A6) yields

$$r'' = \frac{r'(2r^2n^2 + r^3nn' - a^2)}{a\sqrt{r^2n^2 - a^2}}. \quad (\text{A7})$$

By substituting (A6) and (A7) into (A4) and (A5), we arrive at the following expression for bending α :

$$\alpha(a) = -a \int_{x_1}^{x_2} \frac{m' \, dx}{\sqrt{x^2 - a^2}}. \quad (\text{A8})$$

The integrals (A1) and (A8) provide integral representations of the phase delay and bending along a ray, with given impact parameter a between the points r_1 and r_2 as long as the tangent point (or ray perigee) is not between those points ($\beta_1 > 0$). After S and bending angle

α are calculated by numerical integration for a given impact parameter a (computed for a given β_1) and given radii r_1 and r_2 , the central angle θ between the receiver 1 and the transmitter 2 is calculated as

$$\begin{aligned}\theta &= \phi_1 - \phi_2 + \alpha \\ &= \phi_1 - \arcsin\left[\frac{r_1 n(r_1) \sin\phi_1}{r_2}\right] + \alpha,\end{aligned}\quad (\text{A9})$$

which allows us to calculate β_0 :

$$\beta_0 = \arctan\left(\frac{r_2 \cos\theta - r_1}{r_2 \sin\theta}\right), \quad (\text{A10})$$

and S_0 from

$$S_0 = \sqrt{r_1^2 + r_2^2 - 2r_1 r_2 \cos\theta}. \quad (\text{A11})$$

Equations (A10) and (A11) complete the calculation of the excess phase as a function of the geometric elevation angle of the transmitter.

REFERENCES

- Bevis, M. S., S. Businger, T. A. Herring, C. Rocken, R. A. Anthes, and R. H. Ware, 1992: GPS meteorology: Remote sensing of atmospheric water vapor using the Global Positioning System. *J. Geophys. Res.*, **97**, 15 787–15 801.
- Braun, J., C. Rocken, and R. Ware, 2000: Validation of single slant water vapor measurements with GPS. *Radio Sci.*, in press.
- Chen, G., and T. A. Herring, 1997: Effects of atmospheric azimuthal asymmetry on the analysis of space geodetic data. *J. Geophys. Res.*, **102** (B9), 20 489–20 502.
- Davis, J. L., T. A. Herring, I. I. Shapiro, A. E. E. Rogers, and G. Elgered, 1985: Geodesy by radio interferometry: Effects of atmospheric modelling errors on estimates of baseline length. *Radio Sci.*, **20**, 1593–1607.
- Flores, A., G. Ruffini, and A. Rius, 2000: 4D tropospheric tomography using GPS slant wet delay. *Ann. Geophys.*, **18**, 223–234.
- Kalnay, E., and Coauthors, 1996: The NCEP/NCAR 40-Year Reanalysis Project. *Bull. Amer. Meteor. Soc.*, **77**, 437–481.
- Kelso, J. M., 1964: *Radio Ray Propagation in the Ionosphere*. McGraw-Hill, 408 pp.
- Kirchengast, G., J. Hafner, and W. Poetzi, 1999: The CIRA86Q-UoG model: An extension of the CIRA-86 monthly tables including humidity tables and a Fortran95 global moist air climatology model. IMG/U.G Tech. Rep B for ESA/ESTEC, 18 pp.
- Korn, G. A., and T. M. Korn, 1961: *Mathematical Handbook for Scientists and Engineers*. McGraw-Hill, 943 pp.
- Kravtsov, Y. A., and Y. I. Orlov, 1990: *Geometrical Optics of Inhomogeneous Media*. Springer-Verlag, 312 pp.
- MacDonald, A., and Y. Xie, 2000: On the use of slant observations from GPS to diagnose three dimensional water vapor using 3DVAR. Preprints, *Fourth Symp. on Integrated Observing Systems*, Long Beach, CA, Amer. Meteor. Soc., 62–73.
- MacMillan, D. S., and C. Ma, 1994: Evaluation of very long baseline interferometry atmospheric modeling improvements. *J. Geophys. Res.*, **99** (B1), 637–651.
- Matveev, L. T., 1967: *Fundamentals of General Meteorology, Physics of the Atmosphere* (in Russian, translated by IPST). Dept. of Commerce and NSF, 699 pp.
- Niell, A. E., 1996: Global mapping functions for the atmospheric delay at radio wavelengths. *J. Geophys. Res.*, **101**, 3227–3246.
- Owens, J. C., 1967: Optical refractive index of air: Dependence on pressure temperature and composition. *Appl. Opt.*, **6**, 51–58.
- Rocken, C., and Coauthors, 1997a: Analysis and validation of GPS/MET data in the neutral atmosphere. *J. Geophys. Res.*, **102** (D25), 29 849–29 866.
- , T. Van Hove, and R. Ware, 1997b: Near real-time sensing of atmospheric water vapor with GPS. *Geophys. Res. Lett.*, **24**, 3221–3224.
- Saastamoinen, J., 1972: Atmospheric correction for the troposphere and stratosphere in radio ranging of satellites. *The Use of Artificial Satellites for Geodesy, Geophys. Monogr.*, Vol. 15, Amer. Geophys. Union, 247–251.
- Sokolovskiy, S. V., C. Rocken, and A. R. Lowry, 2000: Use of GPS for estimation of bending angles of radio waves at low elevations. *Radio Sci.*, in press.
- Thayer, G. D., 1974: An improved equation for the radio refractive index of air. *Radio Sci.*, **9**, 803–807.
- Ware, R., C. Alber, C. Rocken, and F. Solheim, 1997: Sensing integrated water vapor along GPS ray paths. *Geophys. Res. Lett.*, **24**, 417–420.
- , and Coauthors, 2000: SuomiNet: A real-time national GPS network for atmospheric research and education. *Bull. Amer. Meteor. Soc.*, **81**, 677–694.